Thickness dependence of exchange coupling in (111)-oriented perovskite oxide superlattices

Yue Jia,[1] Rajesh V. Chopdekar,[1] Elke Arenholz,[2] Zhiqi Liu,[3] Michael D. Biegalski,[3] Zachary D. Porter,[4] Apurva Mehta,[4] and Yayoi Takamura[1]

[1]*Department of Chemical Engineering and Materials Science, University of California, Davis, Davis, California 95616, USA*
[2]*Advanced Light Source, Lawrence Berkeley National Laboratory, Berkeley, California 94720, USA*
[3]*Center for Nanophase Materials Science, Oak Ridge National Laboratory, Oak Ridge, Tennessee 37831, USA*
[4]*Stanford Synchrotron Radiation Lightsource, SLAC National Accelerator Laboratory, Menlo Park, California 94025, USA*

(Received 7 December 2015; revised manuscript received 12 February 2016; published 3 March 2016)

Epitaxial $La_{0.7}Sr_{0.3}MnO_3$ (LSMO)/$La_{0.7}Sr_{0.3}FeO_3$ (LSFO) superlattices on (111)-oriented $SrTiO_3$ substrates with sublayer thicknesses ranging from 3 to 60 unit cells (u.c.) were synthesized and characterized. Detailed analysis of their structural, electronic, and magnetic properties were performed to explore the effect of sublayer thickness on the magnetic structure and exchange coupling at (111)-oriented perovskite oxide interfaces. In the ultrathin limit (3–6 u.c.), we find that the antiferromagnetic (AF) properties of the LSFO sublayers are preserved with an out-of-plane canting of the AF spin axis, while the ferromagnetic (FM) properties of the LSMO sublayers are significantly depressed. For thicker LSFO layers (>9 u.c.), the out-of-plane canting of the AF spin axis is only present in superlattices with thick LSMO sublayers. As a result, exchange coupling in the form of spin-flop coupling exists only in superlattices which display both robust ferromagnetism and out-of-plane canting of the AF spin axis.

DOI: 10.1103/PhysRevB.93.104403

I. INTRODUCTION

Exchange coupling between ferromagnetic (FM) and antiferromagnetic (AF) materials has been the focus of experimental and theoretical work since the discovery of exchange bias at Co/CoO interfaces. This form of exchange coupling is characterized by the horizontal shift of the hysteresis loop by the exchange bias field [1,2]. Despite extensive research and incorporation into a wide range of devices, a fundamental understanding of the exchange interactions at FM/AF interfaces is still incomplete. Efforts to develop a comprehensive model to predict the magnitude of the exchange bias field have failed due to the complicated interfacial phenomena [3] involving factors such as surface spins [4], interface roughness [5,6], and the structural and magnetic properties of the FM and AF layers [7,8]. A key aspect of a systematic study investigating exchange coupling is the precise control of the thickness and roughness of the constituent layers of the FM/AF heterostructures, as well as the ability to choose AF layers with different three-dimensional (3D) spin arrangements grown in different crystallographic orientations. In particular, the AF thickness has been shown to be a key parameter impacting the coercivity, exchange bias field, and the blocking temperature [7,9,10]. A critical AF thickness exists below which exchange bias vanishes, and this thickness is closely related to factors such as the AF anisotropy [7], the nature of the exchange interactions across the FM/AF interface, and the spins of the AF and FM interfacial atoms [11].

Unlike metallic FM/AF systems, research on exchange coupling in complex oxide systems is comparatively limited. However, the coupling between the charge, spin, orbital, and lattice degrees of freedom in perovskite oxide heterostructures can offer additional parameters to tune the magnetic properties. With its rich magnetic phase diagram displaying paramagnetic (PM), FM, AF, and spin-canted states [12], the $La_{1-x}Sr_xMnO_3$ system is a prime example to illustrate the complex interactions that can be tailored through parameters such as the doping level (x), epitaxial strain, layer thickness, and crystallographic orientation. For example, $LaMnO_3$/$SrMnO_3$ superlattices consisting of single-unit-cell layers of A-type AF $LaMnO_3$ and G-type AF $SrMnO_3$ were grown to span the FM to AF phases around the $La_{0.5}Sr_{0.5}MnO_3$ composition by careful control of the placement of the A-site cations [13]. In addition, epitaxial strain engineering through the choice of the substrate can tune the orbital polarization of the e_g orbitals of $La_{0.5}Sr_{0.5}MnO_3$, resulting in different AF structures [14]. Finally, the orientation of the films also plays an important role. (001)-oriented $La_{0.7}Sr_{0.3}MnO_3$ (LSMO) films under tensile strain have biaxial anisotropy along the in-plane ⟨110⟩ axes [15], while (111)-oriented LSMO films have low magnetocrystalline anisotropy in the (111) plane with a sixfold symmetry along the $\langle 1\bar{1}0\rangle$ and $\langle \bar{1}\bar{1}2\rangle$ directions [i.e., two low-index families of directions lying within the (111) plane] [16]. Among these tuning parameters, the study of the effect of orientation on the behavior of perovskite oxide thin films has been comparatively limited, with most research being focused on (001)-oriented perovskite heterostructures. This fact is partly due to the difficulty of getting smooth interfaces on other orientations with different dominant growth mechanisms [17]. However, intriguing properties possessed by (111)-oriented perovskite thin films absent in their (001)-oriented counterparts have recently been reported in theoretical and experimental work [18–22]. A buckled honeycomb lattice resembling graphene is formed in the (111) orientation with highly polar stackings, which can yield novel electronic and magnetic behaviors.

In this work, we choose superlattices consisting of alternating layers of FM LSMO and AF $La_{0.7}Sr_{0.3}FeO_3$ (LSFO) as a model system to study the exchange coupling and competing interfacial effects between FM and AF perovskite oxide layers. LSMO is a FM metal with Curie temperature $T_C \sim 360$ K [23]. LSFO is a G-type AF insulator with Néel temperature $T_N \sim 360$ K, with the AF spin axis along the crystallographic $\boldsymbol{a}$ axis [24,25]. According to a simple model, an ideal (001)-oriented LSMO/LSFO interface is characterized by compensated AF

spins such that it experiences spin frustration and minimizes its energy by maintaining a perpendicular orientation between the moments of the FM layer and the AF spin axis [26]. This type of exchange coupling is referred to as *spin-flop coupling* and is characterized by enhanced coercivity and a lack of horizontal shift of the hysteresis loops [2,27,28]. In contrast, for an ideal (111)-oriented LSMO/LSFO interface, the AF spins are fully uncompensated and exchange bias is expected. In our previous study, comparing (001)- and (111)-oriented LSMO/LSFO superlattices with a sublayer thickness of approximately 2 nm, we found that the magnetic structure was sensitive to the crystallographic orientation and that exchange interactions in the form of spin-flop coupling were present in both orientations [29]. In the (001)-oriented LSMO/LSFO superlattices, the ferromagnetism of the LSMO sublayers was suppressed due to charge transfer from Mn^{3+} to Fe^{4+} ions across the interfaces [26], while more robust ferromagnetism and transport behavior were maintained in the (111) orientation. The spin axis of the LSFO layers in the superlattices also changed with the crystal orientation, which lies in the (001) plane in (001)-oriented superlattices and cants out of the (111) plane in (111)-oriented superlattices. In this work we explore the thickness dependence of the magnetic properties and exchange coupling in (111)-oriented LSMO/LSFO superlattices by studying samples with sublayer thicknesses ranging from 0.6 to 13.5 nm. Element specific soft-x-ray magnetic spectroscopy was used to reveal the individual magnetic behaviors of the FM and AF layers as a function of temperature and magnetic field.

II. EXPERIMENTAL PROCEDURE

Epitaxial LSMO and LSFO films and LSMO/LSFO superlattices with sublayer thicknesses ranging from 3 to 60 u.c. (0.6–13.5 nm) were grown on (111)-oriented $SrTiO_3$ (STO) substrates by pulsed laser deposition using a KrF laser (248 nm). A solvent cleaner was used to pre-treat the substrates to remove organic residue from the surface. The notation for the superlattice film stacking is as follows: [number of u.c. LSMO×number of u.c. LSFO] number of repeats, with the LSMO layer grown first on the STO substrate. The [3×3]20, [6×6]10, [9×9]10, and [60×60]1 superlattices, as well as LSMO and LSFO films, were grown with a frequency of 5 Hz (1 Hz) and a fluence of ∼0.5 J cm^{-2} (∼0.9 J cm^{-2}) for the growth of the LSMO (LSFO) layers, respectively. A lower fluence helps to obtain smooth LSMO sublayers in the (111) orientation. During the growth, the substrate temperature was held at 700 °C and the oxygen background pressure was 300 mTorr. The [9×18]5 and [18×18]5 superlattices were grown with a frequency of 10 Hz and a fluence of ∼1.5 J cm^{-2} for both LSMO and LSFO layers with the substrate temperature held at 700 °C and an oxygen background pressure of 200 mTorr. Redundant samples grown with both sets of conditions exhibit the same structural and magnetic properties. The samples were cooled slowly to room temperature after the deposition with an oxygen pressure of 300 Torr to ensure the proper oxygen stoichiometry. The total thickness of the superlattices ranged from 27 to 41 nm.

High-resolution x-ray-diffraction (HRXRD) and resonant x-ray reflectivity (XRR) were carried out to characterize the structural properties using a Bruker D8 DISCOVER four-circle XRD system and Beam Line 2-1 at the Stanford Synchrotron Radiation Lightsource (SSRL). When using a conventional lab x-ray source with Cu $K\alpha$ radiation, the structural analysis is limited by the small density contrast between the LSMO and LSFO layers. To determine the chemical profiles of the superlattices, resonant XRR was performed at energies near the Mn and Fe K edges (6553–6556 eV and 7127 eV, respectively), and away from both of the Mn and Fe absorption edges (8000 and 10 000 eV) as a reference. The sublayer thickness, roughness, and density were obtained by simulating the resonant XRR spectra using the GENX program [30] assuming constant sublayer thickness and interfacial roughness throughout the entire superlattice. A Quantum Design superconducting quantum interface device (SQUID) was used to measure the bulk magnetic properties with the magnetic field applied along the in-plane $[1\bar{1}0]$ and $[\bar{1}\bar{1}2]$ directions. The resistivity was measured using the van der Pauw geometry while warming from 80 K. Soft-x-ray magnetic spectroscopy was performed at 80 K at Beamline 4.0.2 at the Advanced Light Source (ALS) at Lawrence Berkeley Laboratory using total electron yield mode. The detailed measurement geometries will be discussed below.

III. RESULTS AND DISCUSSION

A. Structural characterization

Clear thickness fringes and superlattice peaks are present in the resonant XRR spectra and the symmetric ω-2θ scans measured near the (111) and (222) peaks for the LSMO/LSFO superlattices, indicating their high crystalline quality and low interfacial roughness (see Supplemental Material [31]). The fitting of the resonant XRR spectra for the LSMO/LSFO superlattices indicates that all the superlattices have the as-designed sublayer thickness and smooth interfaces with limited chemical intermixing and diffusion between sublayers. The experimental and simulated spectra as a function of scattering vector for the superlattices are shown in Figs. S1–S6 of the Supplemental Material, with the optimized fit parameters listed in Tables S1–S6. Two individual peaks for LSMO and LSFO, respectively, are present in the $\omega-2\theta$ scans of the bilayer, while the scans of the [3×3]20, [6×6]10, [9×9]10, [18×18]5, and [9×18]5 superlattices show a single zeroth-order superlattice peak. Reciprocal space maps around the (042) and (330) peaks show that all the films and superlattices are fully strained and coherent to the STO substrate (see Supplemental Material). Figure 1 plots the average unit-cell volume of the LSMO/LSFO superlattices, which was calculated based on the in-plane lattice parameter of the STO substrate and zeroth-order superlattice peak from the (222) peak position in the symmetric $\omega-2\theta$ scans. The error bars were derived from the standard deviation of the Gaussian fitting of the zeroth-order superlattice peak. These experimental values were compared to the expected unit-cell volume calculated as the linear combination of the LSMO and LSFO unit-cell volumes determined from the [60×60]1 bilayer as well as the bulk values for LSMO and LSFO assuming pseudocubic lattice parameters of $a_{pc} = 3.87$ Å for LSMO [32] and $a_{pc} = 3.91$ Å for LSFO [33] (horizontal dashed lines). The experimental

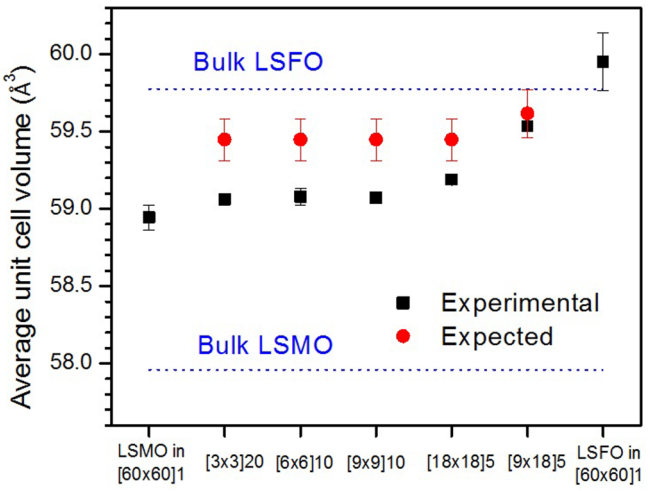

FIG. 1. Experimental and expected values for the average unit-cell volume for the LSMO/LSFO superlattices. The error bars were derived from the standard deviation of the Gaussian fitting of the zeroth-order superlattice peak, while the horizontal dashed lines refer to bulk values for LSMO and LSFO assuming pseudocubic lattice parameters of $a_{pc} = 3.87$ Å for LSMO [31] and $a_{pc} = 3.91$ Å for LSFO [32].

values of the [3×3]20, [6×6]10, [9×9]10, and [18×18]5 superlattices are nearly equal to one another and lower than the expected values, while that of the [9×18]5 superlattice more closely matches the expected value. The fact that the unit-cell volume is not conserved in these epitaxial superlattices indicates that the B-O-B bond lengths and bond angles have deviated away from bulk values, and ultimately are expected to alter the FM and AF properties.

B. Bulk magnetic and electrical properties

The temperature dependence of the magnetization and resistivity of the LSMO film as well as the [9×9]10, [18×18]5, [9×18]5, and [60×60]1 superlattices are plotted in Figs. 2(a) and 2(b). The magnetization curves were measured during warming with a field of 0.01 T applied along the in-plane [1$\bar{1}$0] direction after zero-field cooling from room temperature to 10 K. Since the top layer of the bilayer is 60 u.c. of LSFO, the resistivity is too high to measure; therefore, it is not included. Both the magnetization and the resistivity are normalized to the thickness of the LSMO layers only, rather than to the entire thickness of the superlattice, under the assumption that the insulating AF LSFO sublayers have little contribution to the overall magnetization and conductivity.

The [3×3]20 and [6×6]10 superlattices show insulating and paramagnetic behavior over the entire temperature range of the measurements. In contrast, the magnetization and resistivity curves of the [9×9]10, [9×18]5, [18×18]5, and [60×60]1 superlattices show coincident FM-to-PM and metal-to-insulator transitions, as expected for LSMO, where the magnetic and electrical properties are dictated by the double-exchange mechanism [34–36]. The metal-to-insulator transition temperature T_{MI} is defined as the maximum in $\frac{d\rho}{dT}$. The decrease of the magnetization of the LSMO film at

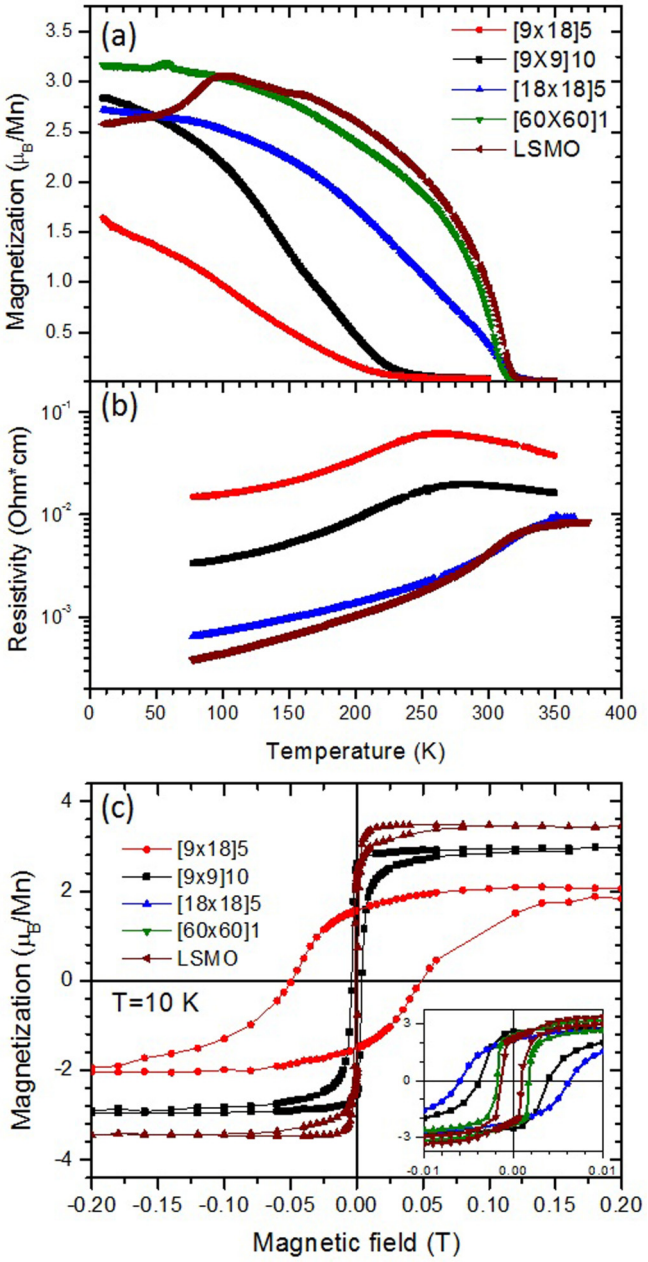

FIG. 2. Temperature dependence of (a) magnetization and (b) resistivity, and (c) SQUID hysteresis loops for the LSMO/LSFO superlattices. The hysteresis loops of the [18×18]5 and [60×60]1 superlattices are very similar to that of the [9×9]10 superlattice thus omitted in the main part of (c). The inset of (c) is a zoomed-up plot of the hysteresis loops in the low-field range.

∼105 K is coincident with the antiferrodistortive transition of the STO substrate from the cubic to tetragonal phase [37], which can change the anisotropy of the LSMO film [38]. The magnetization drop is absent in the superlattices, indicating that the interfacial effects make the superlattices less sensitive to the structural change in the STO substrate. In the limit of thick FM sublayers, the [60×60]1 bilayer and the [18×18]5 superlattice have similar values of $T_C \sim T_{MI} \sim 320$ K to that of the LSMO film, though the M_S is slightly suppressed to $3.2\mu_B$/Mn and $2.9\mu_B$/Mn, respectively, compared to $3.4\mu_B$/Mn for the LSMO film. For thinner FM sublayers

in the [9×9]10 and [9×18]5 superlattices, T_C and T_{MI} are suppressed to ∼230 K while the M_S values are suppressed to $2.9\mu_B$/Mn and $2.1\mu_B$/Mn, respectively. Previous studies on (001)-oriented films and superlattices have attributed the suppression of M_S and T_C in ultrathin films to factors such as interfacial phenomena, including charge transfer [39] and orbital reconstruction [40], eventually leading to the disappearance of ferromagnetism below a critical thickness of 32 Å [38,41]. Charge transfer from Mn^{3+} to Fe^{4+} ions elevates the Mn^{4+}/Mn^{3+} ratio, which is equivalent to a higher Sr doping level with decreased M_S. The LSMO sublayer thickness of the [9×9]10, [18×18]5, and [9×18]5 superlattices is below or near this critical thickness, but due to the difference in the strain state and symmetry of the (111)-orientation, the ferromagnetism remains robust. Although the [9×9]10 and [9×18]5 superlattices have the same FM sublayer thickness, their magnetic and transport behaviors differ dramatically. While the two superlattices share the same T_C value, M_S of the [9×9]10 superlattice is 75% higher than that of the [9×18]5 superlattice, and the resistivity is only ∼1/4 of that of the [9×18]5 superlattice across the temperature range studied. This result suggests that M_S and resistivity are not determined by the sublayer thickness of the FM layer alone, but are also impacted by factors related to the AF sublayers. With varying AF sublayer thickness, the amount of charge transfer and the structural modification to accommodate the electronic and structural difference between LSMO and LSFO can vary, which results in dissimilar magnetic and transport properties.

The hysteresis loops shown in Fig. 2(c) were measured at 10 K after cooling with an applied field of 2 T along the in-plane [1$\bar{1}$0] direction. (111)-oriented LSMO thin films have low magnetocrystalline anisotropy [16] and a low coercive field of 1 mT, which is also the case for the bilayer with a thick LSMO sublayer with a coercive field of 2 mT. In comparison, a coercivity enhancement was found in all three superlattices, which is a signature of exchange coupling, though the lack of horizontal shifts suggests that the form of exchange coupling is not exchange bias. The coercive field of the [9×18]5 superlattice is significantly enhanced to 50 mT compared to ∼5 mT for the [18×18]5 and [9×9]10 superlattices. This increase in coercivity as the relative thickness of AF sublayer increases has been observed in metallic FM/AF systems such as $Ni_{80}Fe_{20}/Fe_{50}Mn_{50}$ bilayers [42] and CoO/Fe bilayers [9]. With increasing sublayer thickness, such as with the [9×18]5 superlattice, the spin configuration of the AF layer becomes more stable due to a greater effective AF anisotropy $K_{AF}t_{AF}$ [43], which in turn provides more effective pinning of the FM layer though exchange coupling. These results demonstrate that the magnetic and transport properties of the LSMO/LSFO superlattices have a complex dependence on both the relative and absolute thickness of the FM and AF sublayers due to the competing interfacial effects, including charge transfer, orbital reconstruction, and epitaxial strain.

C. X-ray magnetic circular dichroism spectroscopy

Element-specific soft-x-ray magnetic spectroscopy was used to differentiate the electronic structure and magnetic properties of the FM and AF layers as a complement to bulk magnetometry measurements. Mn $L_{2,3}$ x-ray-absorption (XA) spectra were acquired at 80 K with the circularly polarized x rays incident at a 30° angle from the sample surface, with the in-plane projection of the x-ray beam along the [1$\bar{1}$2] direction. The x-ray magnetic circular dichroism (XMCD) spectra were calculated as the difference between two XA spectra with a magnetic field of ±0.3 T applied along the x-ray beam direction, and they provide a measure of the atomic spin and orbital magnetic moments. No Fe XMCD was detected within the resolution limit of the measurement in all superlattices, indicating that no or few uncompensated spins exist in the LSFO layers. It should be noted that the (111)-oriented LSMO/LSFO superlattices are distinct from recent reports of FM/nonmagnetic systems where the nonmagnet layer acquires a net magnetic moment at the interface with strong (anti)parallel alignment with the FM moment [44,45]. As will be shown in the following section, this lack of Fe XMCD signal may result from the deviation of the AF spin axis orientation from the bulk structure such that it cants out of the plane of the film. Mn $L_{2,3}$ XA and XMCD spectra of the (111)-oriented LSMO/LSFO superlattices and an LSMO film are shown in Fig. 3. For superlattices with a LSMO sublayer thickness below 9 u.c. (i.e., the [3×3]20 and [6×6]10 superlattices) that display insulating and PM behaviors, a pronounced shoulder peak on the low-energy side of the L_3 peak and a shift of the main L_3 peak towards higher energy can be observed in the XA spectra. These features have been attributed to a higher Mn^{4+}/Mn^{3+} ratio [46,47] and observed in (001)-oriented LSMO/LSFO, $La_{0.6}Sr_{0.4}FeO_3/La_{0.6}Sr_{0.4}MnO_3$, and $LaMnO_3/SrTiO_3$ superlattices resulting from charge transfer

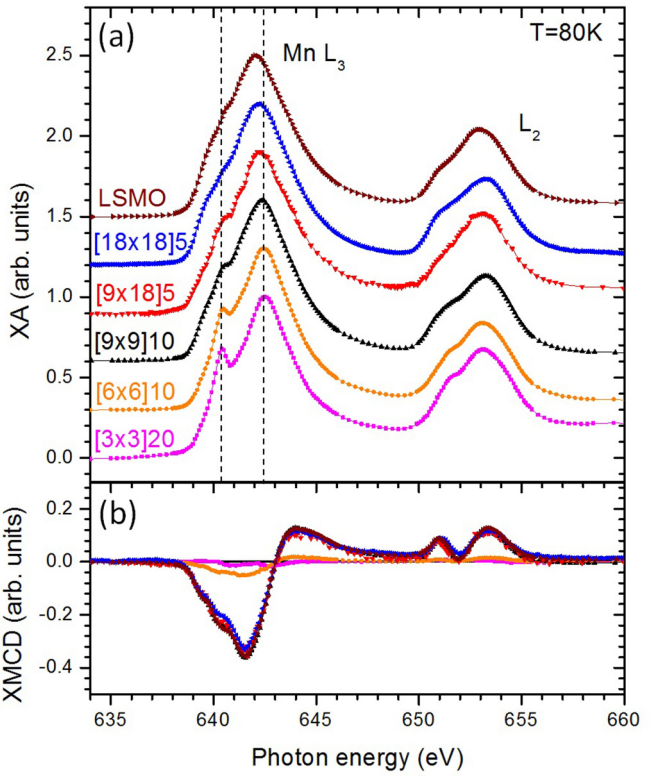

FIG. 3. Mn (a) XA and (b) XMCD spectra for the LSMO/LSFO superlattices, and the LSMO film taken at 80 K.

from Mn^{3+} to Fe^{4+} or Ti^{4+} across the interfaces [26,48,49]. The charge transfer may also be one of the sources of the suppression of T_C and M_S from bulk values, as the magnetic properties of LSMO are mediated by the Mn^{3+}/Mn^{4+} double-exchange mechanism.

D. X-ray magnetic linear dichroism spectroscopy

The magnetic structure of bulk LSFO is G-type AF with the spin axis along the crystallographic $\boldsymbol{a}$ axis [25]. However, in thin-film form, the direction of the spin axis has been shown to vary with growth conditions, strain state, and crystallographic orientation of the film [50,51]. The magnetic structure of the LSFO sublayers in superlattices can further deviate from thin films due to their ultrathin nature, high density of interfaces, and the exchange coupling with FM layers [52]. Previous studies have shown that the LSFO spin axis lies in the plane of the film along the ⟨100⟩ directions in a (001)-oriented [6×6]10 LSMO/LSFO superlattice [26], while it cants out of plane along the ⟨110⟩ directions in a (111)-oriented [9×9]10 LSMO/LSFO superlattice [29]. To study the thickness dependence of the magnetic structure of the AF LSFO layers and the coupling between the AF spins and FM moments, x-ray magnetic linear dichroism (XMLD) spectra were acquired with two measurement geometries.

In geometry 1 [Fig. 4(a)], Fe XMLD spectra were acquired with the x rays at 35° grazing incidence with the in-plane projection of the x-ray beam along the $[\bar{1}\bar{1}2]$ direction and with the magnetic field $\boldsymbol{H} = 0$ after zero-field cooling from room temperature. This measurement geometry minimizes contributions from crystal field effects in the XMLD spectra by choosing two directions from the same family of crystallographic directions. The x-ray polarization $\boldsymbol{E}$ either cants out of plane along the [110] direction or lies in plane along the $[1\bar{1}0]$ direction. The XMLD spectrum is defined as

$$I_{\mathrm{XMLD(1)}} = I_{\mathrm{XA}}(\boldsymbol{E}_{[110]}) - I_{\mathrm{XA}}(\boldsymbol{E}_{[1\bar{1}0]}). \quad (1)$$

This measurement probes whether the AF spin axis lies in plane or cants out of plane. The Fe $L_{2,3}$ XA and XMLD(1) spectra for the LSMO/LSFO superlattices and an LSFO film are shown in Figs. 4(b) and 4(c). The spectra of the [60×60]1 bilayer and the [9×18]5 superlattice have the same shape as that of the LSFO film, which indicates that the spin axis for the two superlattices with thick LSFO sublayers lies in plane [29]. This result agrees with studies on epitaxial $LaFeO_3$ films with thicknesses in the range of 10–100 u.c. on (001)- and (110)-oriented STO substrates, which show that the AF spin axis lies in the pseudocubic (111) plane [50]. In contrast, the sign of the spectra is reversed for the [3×3]20, [6×6]10, and [9×9]10 superlattices with thin LSFO sublayers, suggesting that the spin axis cants out of plane. This canting of the AF axis has been confirmed by soft-x-ray photoemission electron microscopy, where images taken at the Fe L_2 edge showed that strong AF contrast is present only with out-of-plane x-ray polarization [29]. It is noteworthy that the AF order is still preserved at 80 K in [3×3]20 and [6×6]10 with ultrathin LSFO sublayers, even though the ferromagnetism vanishes for LSMO sublayers of equal thickness. As with the FM properties, the superlattices with intermediate sublayer thicknesses display interesting transition behavior. While the

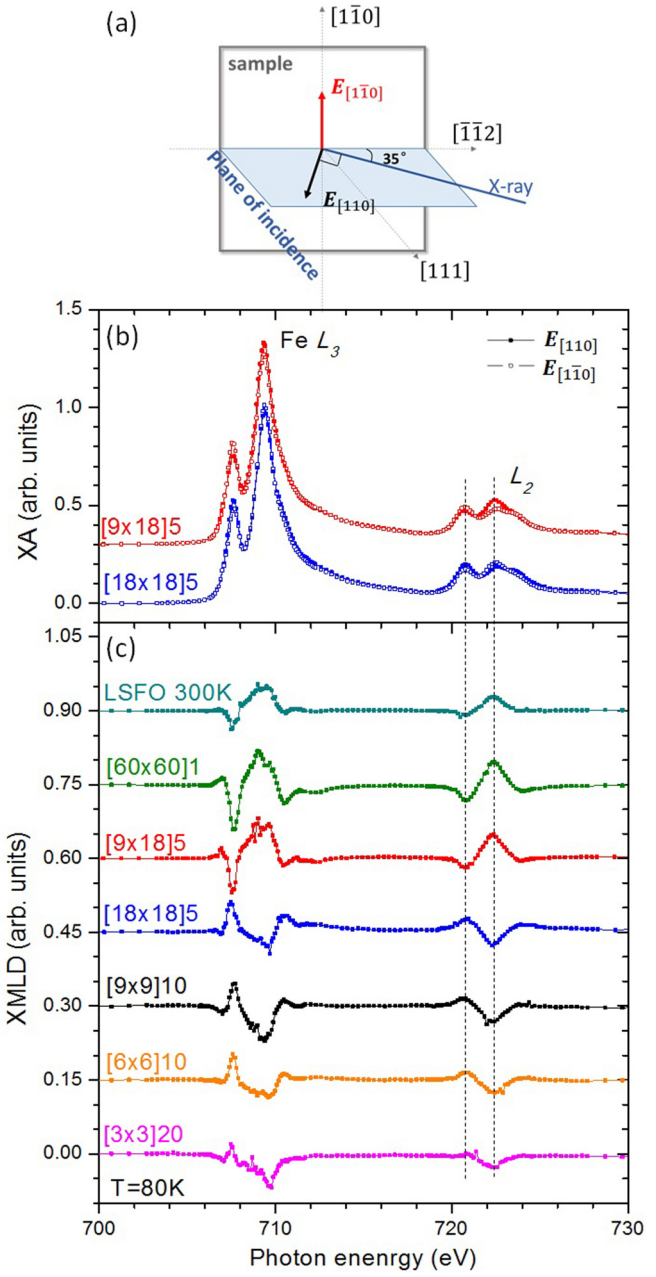

FIG. 4. (a) Schematic of the XMLD(1) measurement geometry; (b) XA and (c) XMLD(1) spectra for the LSMO/LSFO superlattices, and the LSFO film.

[9×18]5 and [18×18]5 superlattices have equivalent LSFO sublayer thickness, the [18×18]5 superlattice behaves like superlattices with thinner LSFO sublayers, where the spin axis cants out of plane. This interfacial spin configuration results from the combined effects of factors such as the anisotropy of the FM and AF layers, the strength of exchange coupling at the top and bottom interfaces of the AF layers, and the presence of defects. Previous experimental [53] and theoretical work [54,55] has shown that an out-of-plane canting of the AF spin axis can minimize the energy difference between parallel and antiparallel configurations between the FM moments and in-plane component of the AF spins. For superlattices with thicker LSMO sublayers, the exchange coupling strength

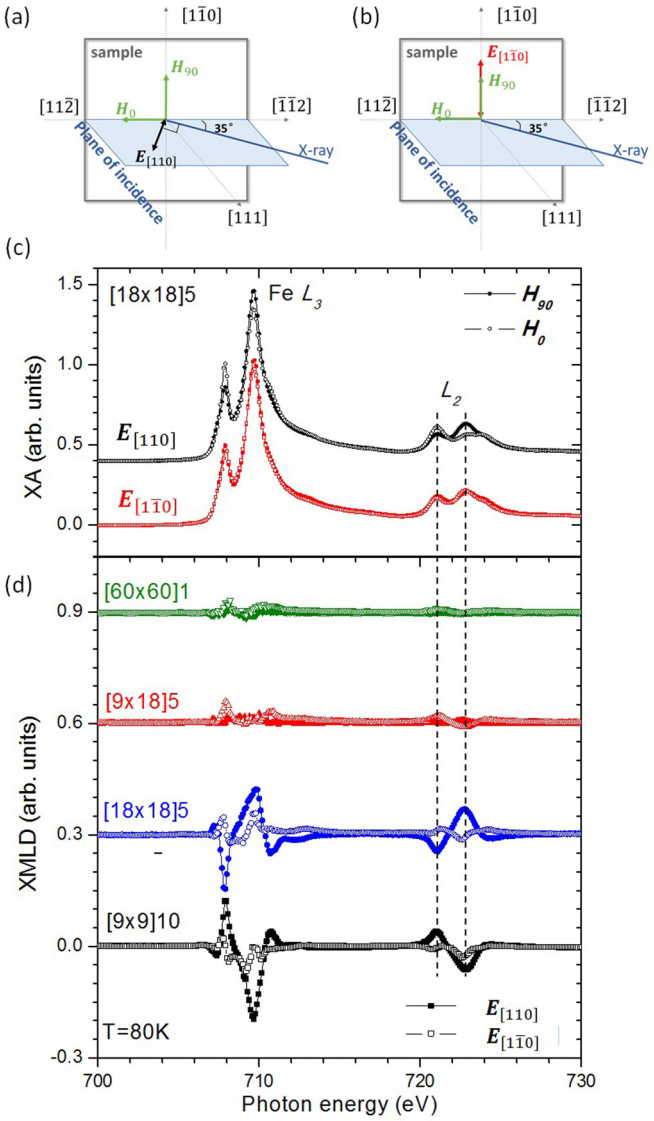

FIG. 5. (a) and (b) Schematics of XMLD(2) measurement geometry. (c) XA spectra for $\boldsymbol{E}$ along the [110] and [1$\bar{1}$0] directions. (d) XMLD(2a) (solid squares) and XMLD(2b) (open squares) spectra for LSMO/LSFO superlattices.

should be considered, and the LSFO spin axis is influenced by the LSMO sublayer thickness. Thus, the canting of the spin axis of the [18×18]5 superlattice with thick FM sublayers with robust ferromagnetism is stabilized by exchange coupling, while the [9×18]5 superlattice with thinner FM sublayers with suppressed ferromagnetism is less influenced by exchange coupling and the AF layers behave more like thick LSFO films.

In geometry 2, Fe XMLD spectra were acquired with the x rays at 35° grazing incidence with the in-plane projection of the x-ray beam along the [1$\bar{1}$2] direction with the fixed x-ray polarization $\boldsymbol{E}$ either canting out of plane along the [110] direction [geometry 2a, Fig. 5(a)] or lying in plane along the [1$\bar{1}$0] direction [geometry 2b, Fig. 5(b)]. A magnetic field of $\boldsymbol{H} = 0.3$ T was applied along the [11$\bar{2}$] or [1$\bar{1}$0] direction, defined as $\boldsymbol{H}_0$ and $\boldsymbol{H}_{90}$, respectively. For the field, a canting angle of 30° relative to the sample surface was used to increase the electron yield signal. The XMLD(2) spectra are defined as

$$I_{\mathrm{XMLD(2a)}} = I_{\mathrm{XA}}(\boldsymbol{E}_{[110]}, \boldsymbol{H}_{90}) - I_{\mathrm{XA}}(\boldsymbol{E}_{[110]}, \boldsymbol{H}_0) \quad (2)$$

and

$$I_{\mathrm{XMLD(2b)}} = I_{\mathrm{XA}}(\boldsymbol{E}_{[1\bar{1}0]}, \boldsymbol{H}_{90}) - I_{\mathrm{XA}}(\boldsymbol{E}_{[1\bar{1}0]}, \boldsymbol{H}_0). \quad (3)$$

These measurements probe how the out-of-plane (geometry 2a) and in-plane (geometry 2b) components of the AF spins react to the external magnetic field through exchange coupling with the FM moments. The applied magnetic field aligns the Mn moments either parallel with or perpendicular to the in-plane projection of the x-ray polarization $\boldsymbol{E}$. Figures 5(c) and 5(d) plot the Fe $L_{2,3}$ XA and XMLD spectra for the [9×9]10, [18×18]5, [9×18]5, and [60×60] superlattices measured with the two variants of geometry 2. For the [9×9]10 and [18×18]5 superlattices, significant XMLD signals can be obtained with both out-of-plane and in-plane $\boldsymbol{E}$ orientations, which indicates that the AF spins are spin-flop coupled to the FM moments and can be reoriented by a moderate magnetic field. The XMLD(2a) signal is distinctively higher than that of XMLD(2b), since for the two superlattices the AF spin axis cants out of plane and XMLD(2b) can only probe the response of the in-plane projection. The sign of the XMLD spectra is reversed between the [9×9]10 and [18×18]5 superlattices, which we attribute to the difference in preferred spin axis directions. In contrast, the [9×18]5 superlattice has little XMLD signal, which suggests that the majority of the AF spins are frozen to the preferred crystallographic directions. The FM layers are too thin relative to the AF layers to have strong coupling to reorient all the AF spins. The small XMLD signal may come from the reorientation of the interfacial AF spins through the Fe-O-Mn interaction, which only accounts for a small portion of the total AF spins, and the majority of the LSFO sublayer retains the same properties of a thick LSFO film. The FM moments in the superlattice are stabilized by the thick AF sublayers, which makes the FM sublayers magnetically harder, as indicated by the hysteresis loops [Fig. 2(c)] obtained by SQUID magnetometry. Similar effects have been observed in (111)-oriented $LaMnO_3$/$LaFeO_3$ superlattices [21]. The correlation length of the spins should be a function of both FM and AF sublayer thicknesses, because the anisotropy is dependent on the thickness and it influences the exchange coupling strength. For the [60×60]1 bilayer, both XMLD(2a) and XMLD(2b) signals are negligible, suggesting that the AF spins cannot be reoriented by a moderate magnetic field, which is usually the case for AF materials. This also rules out the possibility that the XMLD(2) signal comes from other instrumental effects rather than the reorientation of Fe moments.

To further confirm the cooperative reorientation of the FM moments and AF spins, Mn L_3 XMCD and Fe L_2 XMLD hysteresis loops were measured for the [9×9]10, [18×18]5, [9×18]5, and [60×60]1 superlattices, and are plotted in Figs. 6(a)–6(d). For the Mn XMCD hysteresis loops, the measurement geometry is the same as that for the XMCD measurement described above. The asymmetry values were determined as the difference between the absorption values of right and left circularly polarized x rays at the

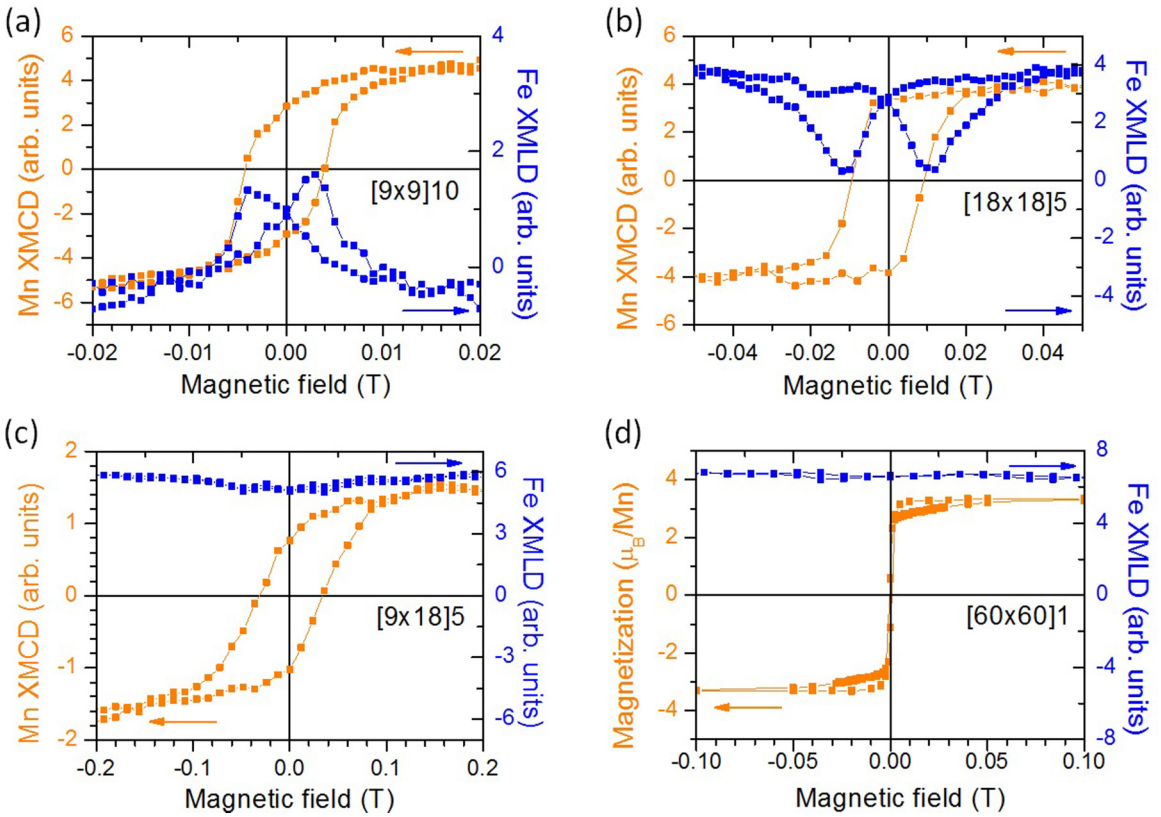

FIG. 6. Mn XMCD and Fe XMLD hysteresis loops for the (a) [9×9]10, (b) [18×18]5, (c) [9×18]5, and (d) [60×60]1 superlattices.

photon energy corresponding to the maximum in XMCD, and then normalized to the sum. For the Fe XMLD loops, the measurement geometry is the same as XMLD geometry 1 with the varying magnetic field applied along the x-ray beam. The asymmetry values were determined as the difference between the absorption values of the out-of-plane and in-plane $\boldsymbol{E}$ vectors at the photon energy corresponding to the Fe L_{2b} peak. Since the top LSFO layer of the [60×60]1 bilayer is too thick to measure, a Mn XMCD hysteresis loop–the hysteresis loop obtained by SQUID magnetometry–is plotted in Fig. 6(d) for comparison. The peaks of the Fe XMLD loops of the [9×9]10 and [18×18]5 superlattices match well with the coercive field of the Mn XMCD loops, indicating that AF spins rotate during the reversal of the Mn moments. For the [9×18]5 and [60×60]1 superlattices, the absence of the Fe XMLD loop suggests that the AF spins are frozen during the magnetization reversal of LSMO layers.

IV. CONCLUSIONS

In summary, the thickness dependence of the magnetic interactions in (111)-oriented LSMO/LSFO superlattices has been studied. It was found that the transport properties, magnetic structure, and nature of the exchange coupling were influenced not only by the absolute thickness of the LSMO and LSFO sublayers, but also by the relative thickness of the FM and AF layers. The findings are summarized in the phase diagram shown in Fig. 7. In the limit of thick LSFO sublayers, the AF behavior matches that of bulk LSFO with the AF spin axis fixed in the pseudocubic (111) plane. Below a critical thickness, (∼20 u.c.), the sublayers become too thin

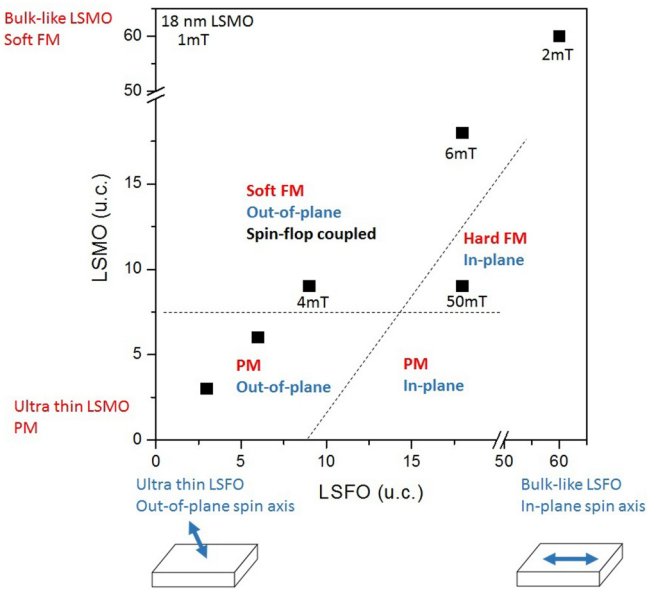

FIG. 7. Phase diagram of the magnetic properties of (111)-oriented LSMO/LSFO superlattices as a function of LSMO and LSFO layer thickness. The FM/PM properties are indicated in red text, the coercive field in black, and the direction of the AF spin axis in blue. The dashed lines are visual guides indicating boundaries between different magnetic phases.

to be safely assumed to be bulklike. In this case, when the LSMO and LSFO sublayer thicknesses are comparable, robust ferromagnetism is present, the spin axis of LSFO cants out of plane of the film, and it can be reoriented by a moderate external magnetic field through spin-flop coupling with the magnetically soft LSMO sublayers. However, if the LSFO sublayer thickness exceeds that of the LSMO sublayers, the LSMO sublayers become pinned by the LSFO sublayers, increasing the coercivity, while the AF spin axis lies in plane and cannot be reoriented by a moderate external magnetic field like a thick LSFO single layer. For the superlattices with ultrathin LSMO and LSFO sublayers (3–6 u.c.), the ferromagnetism vanishes due to charge transfer across the interface, and the AF spin axis cants out of plane.

ACKNOWLEDGMENTS

This work was supported by the Semiconductor Research Corporation under Task No. 2309.001. The Advanced Light Source, Lawrence Berkeley Laboratory, is supported by the Director, Office of Science, Office of Basic Energy Sciences, of the U.S. Department of Energy under Contract No. DE-AC02-05CH11231. Use of the Stanford Synchrotron Radiation Lightsource, SLAC National Accelerator Laboratory, is supported by the U.S. Department of Energy, Office of Science, Office of Basic Energy Sciences, under Contract No. DE-AC02-76SF00515. Part of the sample fabrication of this research was conducted at the Center for Nanophase Materials Sciences, a U.S. DOE Office of Science User Facility.

[1] W. H. Meiklejohn and C. P. Bean, Phys. Rev. **102**, 1413 (1956).
[2] J. Nogues, J. Sort, V. Langlais, V. Skumryev, S. Surinach, J. S. Munoz, and M. D. Baro, Phys. Rep. **422**, 65 (2005).
[3] M. Kiwi, J. Magn. Magn. Mater. **234**, 584 (2001).
[4] H. Ohldag, A. Scholl, F. Nolting, E. Arenholz, S. Maat, A. T. Young, M. Carey, and J. Stöhr, Phys. Rev. Lett. **91**, 017203 (2003).
[5] M. D. Stiles and R. D. McMichael, Phys. Rev. B **59**, 3722 (1999).
[6] W. Kuch, L. I. Chelaru, F. Offi, J. Wang, M. Kotsugi, and J. Kirschner, Nat. Mater. **5**, 128 (2006).
[7] M. S. Lund, W. A. A. Macedo, K. Liu, J. Nogués, I. K. Schuller, and C. Leighton, Phys. Rev. B **66**, 054422 (2002).
[8] S. Maat, K. Takano, S. S. P. Parkin, and E. E. Fullerton, Phys. Rev. Lett. **87**, 087202 (2001).
[9] J. Wu, J. S. Park, W. Kim, E. Arenholz, M. Liberati, A. Scholl, Y. Z. Wu, C. Hwang, and Z. Q. Qiu, Phys. Rev. Lett. **104**, 217204 (2010).
[10] T. Ambrose and C. L. Chien, J. Appl. Phys. **83**, 6822 (1998).
[11] C. Binek, A. Hochstrat, and W. Kleemann, J. Magn. Magn. Mater. **234**, 353 (2001).
[12] Y. Tokura and Y. Tomioka, J. Magn. Magn. Mater. **200**, 1 (1999).
[13] T. S. Santos, S. J. May, J. L. Robertson, and A. Bhattacharya, Phys. Rev. B **80**, 155114 (2009).
[14] W. B. Wu, D. J. Huang, C. M. Huang, C. H. Hsu, C. F. Chang, H. J. Lin, and C. T. Chen, J. Magn. Magn. Mater. **310**, 813 (2007).
[15] L. M. Berndt, V. Balbarin, and Y. Suzuki, Appl. Phys. Lett. **77**, 2903 (2000).
[16] I. Hallsteinsen, E. Folven, F. K. Olsen, R. V. Chopdekar, M. S. Rzchowski, C. B. Eom, J. K. Grepstad, and T. Tybell, Appl. Phys. Lett. Mater. **3**, 062501 (2015).
[17] I. Hallsteinsen, J. E. Boschker, M. Nord, S. Lee, M. Rzchowski, P. E. Vullum, J. K. Grepstad, R. Holmestad, C. B. Eom, and T. Tybell, J. Appl. Phys. **113**, 183512 (2013).
[18] M. Gibert, P. Zubko, R. Scherwitzl, J. Íñiguez, and J.-M. Triscone, Nat. Mater. **11**, 195 (2012).
[19] D. Doennig, W. E. Pickett, and R. Pentcheva, Phys. Rev. Lett. **111**, 126804 (2013).
[20] K. Ueda, Science **280**, 1064 (1998).
[21] K. Ueda, H. Tabata, and T. Kawai, Phys. Rev. B **60**, R12561(R) (1999).
[22] A. Grutter, F. Wong, E. Arenholz, M. Liberati, A. Vailionis, and Y. Suzuki, Appl. Phys. Lett. **96**, 082509 (2010).
[23] A. Urushibara, Y. Moritomo, T. Arima, A. Asamitsu, G. Kido, and Y. Tokura, Phys. Rev. B **51**, 14103 (1995).
[24] U. Shimony and J. M. Knudsen, Phys. Rev. **144**, 361 (1966)
[25] R. L. White, J. Appl. Phys. **40**, 1061 (1969).
[26] Y. Takamura, F. Yang, N. Kemik, E. Arenholz, M. D. Biegalski, and H. M. Christen, Phys. Rev. B **80**, 180417(R) (2009).
[27] M. Finazzi, M. Portalupi, A. Brambilla, L. Duo, G. Ghiringhelli, F. Parmigiani, M. Zacchigna, M. Zangrando, and F. Ciccacci, Phys. Rev. B **69**, 014410 (2004).
[28] N. C. Koon, Phys. Rev. Lett. **78**, 4865 (1997).
[29] Y. Jia, R. V. Chopdekar, E. Arenholz, A. T. Young, M. A. Marcus, A. Mehta, and Y. Takamura, Phys. Rev. B **92**, 094407 (2015).
[30] M. Bjorck and G. Andersson, J. Appl. Crystallogr. **40**, 1174 (2007).
[31] See Supplemental Material at http://link.aps.org/supplemental/10.1103/PhysRevB.93.104403 for the experimental and simulated resonant XRR spectra and the symmetric ω-2θ scans near the (222) peak of the superlattices, the LSMO and LSFO films.
[32] P. G Radaelli, G. Iannone, M. Marezio, H. Y Hwang, S. W. Cheong, J. D. Jorgensen, and D. N. Argyriou, Phys. Rev. B **56**, 8265 (1997).
[33] A. Fossdal, M. Menon, I. Waernhus, K. Wiik, M. A. Einarsrud, and T. Grande, J. Am. Ceram. Soc. **87**, 1952 (2004).
[34] P. de Gennes, Phys. Rev. **118**, 141 (1960).
[35] P. Anderson and H. Hasegawa, Phys. Rev. **100**, 675 (1955).
[36] A. J. Millis, P. B. Littlewood, and B. I. Shraiman, Phys. Rev. Lett. **74**, 5144 (1995).
[37] J. C. Slonczewski and H. Thomas, Phys. Rev. B **1**, 3599 (1970).
[38] R. V. Chopdekar, E. Arenholz, and Y. Suzuki, Phys. Rev. B **79**, 104417 (2009).
[39] R. Hashimoto, A. Chikamatsu, H. Kumigashira, M. Oshima, N. Nakagawa, T. Ohnishi, M. Lippmaa, H. Wadati, A. Fujimori, K. Ono, M. Kawasaki, and H. Koinuma, J. Electron. Spectrosc. Relat. Phenom. **144**, 479 (2005).
[40] A. Tebano, C. Aruta, S. Sanna, P. G. Medaglia, G. Balestrino, A. A. Sidorenko, R. De Renzi, G. Ghiringhelli, L. Braicovich, V. Bisogni, and N. B. Brookes, Phys. Rev. Lett. **100**, 137401 (2008).
[41] M. Huijben, L. W. Martin, Y. H. Chu, M. B. Holcomb, P. Yu, G. Rijnders, D. H. A. Blank, and R. Ramesh, Phys. Rev. B **78**, 094413 (2008).
[42] R. Jungblut, R. Coehoorn, M. T. Johnson, J. aan de Stegge, and A. Reinders, J. Appl. Phys. **75**, 6659 (1994).

[43] J. Nogués and I. K. Schuller, J. Magn. Magn. Mater. **192**, 203 (1999).
[44] C. Piamonteze, M. Gibert, J. Heidler, J. Dreiser, S. Rusponi, H. Brune, J. M. Triscone, F. Nolting, and U. Staub, Phys. Rev. B **92**, 014426 (2015).
[45] F. Y. Bruno, M. N. Grisolia, C. Visani, S. Valencia, M. Varela, R. Abrudan, J. Tornos, A. Rivera-Calzada, A. A. Ünal, S. J. Pennycook, Z. Sefrioui, C. Leon, J. E. Villegas, J. Santamaria, A. Barthélémy, and M. Bibes, Nat. Commun. **6**, 6306 (2015).
[46] M. Abbate, F. de Groot, J. Fuggle, A. Fujimori, O. Strebel, F. Lopez, M. Domke, G. Kaindl, G. Sawatzky, M. Takano, Y. Takeda, H. Eisaki, and S. Uchida, Phys. Rev. B **46**, 4511 (1992).
[47] F. M. F. de Groot, J. Electron. Spectrosc. Relat. Phenom. **67**, 529 (1994).
[48] H. Kumigashira, D. Kobayashi, R. Hashimoto, A. Chikamatsu, M. Oshima, N. Nakagawa, T. Ohnishi, M. Lippmaa, H. Wadati, A. Fujimori, K. Ono, M. Kawasaki, and H. Koinuma, Appl. Phys. Lett. **84**, 5353 (2004).
[49] J. Garcia-Barriocanal, J. C. Cezar, F. Y. Bruno, P. Thakur, N. B. Brookes, C. Utfeld, A. Rivera-Calzada, S. R. Giblin, J. W. Taylor, J. A. Duffy, S. B. Dugdale, T. Nakamura, K. Kodama, C. Leon, S. Okamoto, and J. Santamaria, Nat. Commun. **1**, 82 (2010).
[50] J. Lüning, F. Nolting, A. Scholl, H. Ohldag, J. W. Seo, J. Fompeyrine, J. P. Locquet, and J. Stöhr, Phys. Rev. B **67**, 214433 (2003).
[51] S. Czekaj, F. Nolting, L. J. Heyderman, P. R. Willmott, and G. van der Laan, Phys. Rev. B **73**, 020401 (2006).
[52] E. Arenholz, G. van der Laan, F. Yang, N. Kemik, M. D. Biegalski, H. M. Christen, and Y. Takamura, Appl. Phys. Lett. **94**, 072503 (2009).
[53] J. Nogués, T. J. Moran, D. Lederman, I. K. Schuller, and K. V. Rao, Phys. Rev. B **59**, 6984 (1999).
[54] A. P. Malozemoff, Phys. Rev. B **35**, 3679 (1987).
[55] A. P. Malozemoff, J. Appl. Phys. **63**, 3874 (1988).